arXiv:1609.09112v2 [astro-ph.GA] 3 Oct 2016

Energy budget of forming clumps in numerical simulations of collapsing clouds

Vianey Camacho[1], Enrique Vázquez-Semadeni[1], Javier Ballesteros-Paredes[1], Gilberto C. Gómez[1], S. Michael Fall[2], M. Dolores Mata-Chávez[1]

1. Instituto de Radioastronomía y Astrofísica,
Universidad Nacional Autónoma de México, Campus Morelia
Apartado Postal 3-72, 58090, Morelia, Michoacán, México
2. Space Telescope Science Institute
3700 San Martin Drive
Baltimore, MD 21218 US

ABSTRACT

We analyze the physical properties and energy balance of density enhancements in two SPH simulations of the formation, evolution, and collapse of giant molecular clouds. In the simulations, no feedback is included, so all motions are due either to the initial, decaying turbulence, or to gravitational contraction. We define clumps as connected regions above a series of density thresholds. The resulting full set of clumps follows the generalized energy-equipartition relation $\sigma_v/R^{1/2} \propto \Sigma^{1/2}$, where σ_v is the velocity dispersion, R is the 'radius", and Σ is the column density. We interpret this as a natural consequence of gravitational contraction at all scales, rather than virial equilibrium. Nevertheless, clumps with low Σ tend to show a large scatter around equipartition. In more than half of the cases, this scatter is dominated by external turbulent compressions that *assemble* the clumps, rather than by small-scale random motions that would disperse them. The other half does actually disperse. Moreover, clump sub-samples selected by means of different criteria exhibit different scalings. Sub-samples with narrow Σ ranges follow Larson-like relations, although characterized by their respective value of Σ. Finally, we find that: i) clumps lying in filaments tend to appear sub-virial; ii) high-density cores ($n \geq 10^5$ cm^3) that exhibit moderate kinetic energy excesses often contain sink ("stellar") particles, and the excess disappears when the stellar mass is taken into account in the energy balance; iii) cores with kinetic energy excess but no stellar particles are truly in a state of dispersal.

Subject headings: - - - -

1. Introduction

Ever since the pioneering work of Larson (1981) it has been recognized that molecular clouds (MCs) obey scaling relationships, that have been interpreted as representative of approximate virial equilibrium in the clouds between their internal "turbulent" motions and their self-gravity. Subsequently, however, there have been suggestions that these relations may actually be the result of observational selection effects (e.g., Kegel 1989; Scalo 1990). In addition, there have been attempts at generalization of these relations (e.g., Keto & Myers 1986; Heyer et al. 2009) and reinterpretations in terms of global cloud collapse rather than virialization (Ballesteros-Paredes et al. 2011, hereafter B11). Moreover, there are structures that are observed to possess kinetic energies in excess of those that would be consistent with equilibrium (or more generally, energy equipartition).

In this paper we aim to investigate whether clumps forming in numerical simulations of clouds undergoing global gravitational contraction ex-

hibit similar properties as those in observational surveys such as Larson scaling relations, and search for a cause of the apparent kinetic energy excesses seen in some subsets of clumps in observational samples.

1.1. Larson's relations and their generalization

For over three decades, it has been accepted that molecular clouds (MCs) satisfy the so-called Larson (1981) scaling relations between velocity dispersion ($\sigma_{\rm v}$), mean number density ($\langle n \rangle$) and size (L). In their presently accepted form, these relations are (e.g., Solomon et al. 1987; Heyer & Brunt 2004)

$$\langle n \rangle \approx 3400 \left(\frac{L}{1\,{\rm pc}} \right)^{-1} \ {\rm cm}^{-3}, \tag{1}$$

and

$$\sigma_{\rm v} \approx 1 \left(\frac{L}{1\,{\rm pc}} \right)^{1/2} \ {\rm km\ s}^{-1}. \tag{2}$$

Larson (1981) additionally showed that these relations implied that the velocity dispersion is close to the value corresponding to virial equilibrium. In what follows, we will more generally refer to this as "near equipartition" between the nonthermal kinetic and the gravitational energies. Also, it should be remarked that eq. (1) implies that the column density of the clouds, $\Sigma = \int_{\rm LOS} \rho d\ell$ is approximately the same for MCs of all sizes. In this expression, ℓ is the length element, and the integration is performed along the line-of-sight (LOS) through the cloud.

However, the validity of Larson's relations has been questioned by various authors. Kegel (1989) and Scalo (1990) argued that the apparent constancy of the column density may arise from selection effects caused by the need to exceed a certain minimum column density in order to detect the clouds, and by a maximum apparent column density caused by line saturation (optical thickening). This possibility was in fact recognized by Larson (1981) himself. Some time later, Ballesteros-Paredes & Mac Low (2002) showed that, in numerical simulations of turbulent clouds, clumps defined by means of a column density threshold exhibited a Larson-like density-size relation, but clumps defined by means of a *volume* density threshold did not.

Several years later, using the Boston University-FCRAO Galactic Ring Survey (Jackson et al. 2006), Heyer et al. (2009, hereafter H09) reanalyzed the giant molecular cloud (GMC) sample of Solomon et al. (1987). The higher angular sampling rate and resolution available to H09, as well as the use of the ^{13}CO $J = 1$–0 line allowed them to obtain a much larger dynamic range in column density than that available to Solomon et al. (1987). Moreover, H09 considered two different definitions for the cloud boundaries, thus effectively obtaining two different MC samples.[1] With this procedure, the GMC sample of H09 spanned over two orders of magnitude in column density, making it clear that column density is *not* constant for GMCs (see also Heyer et al. 2001). Nevertheless, H09 noted that, in spite of the non-constancy of the column density, the GMCs are still consistent with virial equilibrium. They showed this by noting that their GMC sample satisfied

$$\frac{\sigma_{\rm v}}{R^{1/2}} \approx \left(\frac{\pi G \Sigma}{5} \right)^{1/2}. \tag{3}$$

When the column density is not constant, this relationship corresponds to virial equilibrium; i.e., to $|E_{\rm g}| = 2E_{\rm k}$, with $E_{\rm k}$ being the nonthermal kinetic energy and $E_{\rm g}$ being the gravitational energy for a spherical cloud of uniform density and radius R. Thus, eq. (3) can be considered as the generalization of Larson's relations when Σ is not constant.

Shortly thereafter, Lombardi et al. (2010) claimed that the column density of GMCs is constant after all. Using near-infrared excess techniques, these authors argued that the mean GMC column density in their sample remained constant in spite of being sensitive to very low extinctions, thus suggesting that the minimum-column density imposed by a sensitivity threshold was not an issue. However, it has subsequently been recognized that this effect is natural for clouds with a Σ probability density function (PDF) that peaks at some value and drops fast enough at lower column densities

[1] Contrary to some claims in the literature, these two definitions of the cloud boundaries do amount to *two* different MC samples, as the masses and velocity dispersions were measured for each cloud within each of the two boundaries. Thus, the 'A2' clouds in H09 constitute a sample of smaller, denser objects within the 'A1' sample, just like dense clumps and cores are substructures of their parent MCs, with independent dynamical indicators.

(Beaumont et al. 2012; Ballesteros-Paredes et al. 2012). The lack of pixels at low Σ implies that the dominant apparent column density will be that of the peak, and it is now recognized that the presence of a peak may be an artifact of incomplete sampling at low column densities (Lombardi et al. 2015). Therefore, at present there is no compelling evidence for the validity of the density-size relation (eq. 1) for GMCs nor their substructures in general.

On the other hand, the velocity dispersion-size relation,[2] expression (2) above, has often been interpreted as the signature of supersonic turbulence, with an energy spectrum $E(k) \propto k^{-2}$, where k is the wavenumber. Indeed, the velocity variance, interpreted as the average turbulent kinetic energy per unit mass in scales of size $\ell \leq 2\pi/k$, given by $\sigma_{\rm v}^2(\ell) = \int_{k>2\pi/\ell} E(k)dk$, scales as $\ell^{1/2}$ (e.g. Vázquez-Semadeni et al. 2000a; Elmegreen & Scalo 2004; McKee & Ostriker 2007). In this case, the velocity dispersion- size relation would have a completely independent origin from that of the density-size relation, and the reason for the observed near- equipartition between the gravitational and turbulent kinetic energies would require a separate explanation. However, massive star-forming clumps notoriously do not conform to the $\sigma_{\rm v}$-L relation (e.g., Caselli & Myers 1995; Plume et al. 1997; Shirley et al. 2003; Gibson et al. 2009; Wu et al. 2010), a situation that appears inconsistent with a universal turbulent energy cascade spanning the whole range from the scale of GMCs down to the scale of massive clumps.

An alternative interpretation was suggested by Ballesteros-Paredes et al. (2011, hereafter B11), who proposed that the origin of the $\sigma_{\rm v}$-L relation was not turbulence, but rather gravitational contraction of the clouds, combined with the observational selection effect of a restricted column density range. This possibility was actually suggested over four decades ago by Goldreich & Kwan (1974). Similarly, Liszt et al. (1974) suggested that their line profiles and LOS-velocity maps of the Orion MC were consistent with extended radial motions, although they could not discriminate between expansion and collapse. However, the extended-motion scenario was soon dismissed by Zuckerman & Palmer (1974), who argued that, if that were the case, then the star formation rate in MCs should be much larger than observed, and that systematic shifts between emission lines produced by HII regions at the centers of the clouds and absorption lines produced in the radially- moving cloud envelopes should be observed, but they are not. Zuckerman & Evans (1974) then proposed that the observed linewidths corresponded to supersonic, small-scale turbulence.

The small-scale turbulence scenario, however, suffers from a number of problems (see Vázquez-Semadeni 2015, for a detailed discussion). Instead, B11 have suggested a return to the scenario of gravitational collapse at the scale of the whole GMCs, with the problem of an excessive SFR being solved by early destruction of the clouds by stellar feedback (Vázquez-Semadeni et al. 2010; Zamora-Avilés et al. 2012; Dale et al. 2012; Colín et al. 2013; Zamora-Avilés & Vázquez-Semadeni 2014). B11 noted that the generalized Larson relation, eq. (3) is not only satisfied by GMCs, but also by massive clumps that do not satisfy Larson's velocity dispersion-size relation, eq. (2).

Thus, B11 interpreted the near-equipartition as evidence for free-fall in the clouds (see also Traficante et al. 2015) rather than near-virial equilibrium, noting that the virial and free-fall velocities differ only by a factor of $\sqrt{2}$. Indeed, for a freely collapsing cloud, defining the total energy as zero, the nonthermal kinetic energy and the gravitational energy satisfy $E_{\rm k} = |E_{\rm g}|$, so that, instead of eq. (3), we have

$$\frac{\sigma_{\rm v}}{R^{1/2}} \approx \left(\frac{2\pi G\Sigma}{5}\right)^{1/2}. \qquad (4)$$

Generally, the observational errors and uncertainties in cloud and clump surveys are larger than this slight $\sqrt{2}$ factor, so that, for all practical purposes, *any evidence in favor of virial equilibrium based on energetics of the clouds can just as well be interpreted as evidence in favor of free collapse.* Recent observational studies have shown signatures of infall motions in line profiles along filaments and massive clumps in the Cygnus X region (Schneider et al. 2010), in massive star-forming cores of the infrared dark cloud SDC335.579-0.272 (Peretto et al. 2013), and in

[2] In what follows, we will refer to this relation as the linewidth-size relation as well.

massive starless cores (Traficante et al. 2015), supporting the notion that this systems are consistent with a global gravitational collapse. Moreover, Traficante et al. (2015) introduce an equivalent analysis as in H09 to demonstrate that most of the non-thermal motions in their sample originate from self-gravity.

1.2. Deviations from energy equipartition

An additional important feature in the GMC sample studied by H09 is that the clouds tended to lie systematically *above* the virial-equilibrium line in a plot of $\sigma_{\rm v}/R^{1/2}$ *vs.* Σ, a plot that we will refer to as the Keto-Heyer or KH diagram (Keto & Myers 1986; Heyer et al. 2009). This feature has received different interpretations by different authors. H09 themselves interpreted it simply as a systematic underestimation of the cloud masses, due to the various assumptions they used in determining the masses from ^{13}CO emission. On the other hand, Dobbs et al. (2011) have interpreted this feature as evidence that most of the GMCs are gravitationally unbound, probably because they form by cloud-cloud collisions, which feed a large velocity dispersion that unbinds the GMCs. Keto & Myers (1986) and Field et al. (2011), instead, have assumed that the clouds are gravitationally unbound, but confined by an external pressure, while B11 suggested that the GMCs are actually collapsing, and that, at face value, the H09 data are slightly more consistent with free-fall than with virial equilibrium, since the free-fall velocity is slightly larger than the virial one.

In addition to the slight systematic overvirial nature of cloud surveys, in several observational clump and core surveys, some objects appear to be *strongly* overvirial, exhibiting values of the *virial parameter*, $\alpha \equiv 5\sigma_{\rm v}^2 R/GM \sim 10$–$100$ (see,e.g., fig. 16 of Barnes et al. 2011), especially in the case of low-mass objects. These objects are traditionally interpreted as having a kinetic energy significantly larger than their gravitational energy, perhaps due to driving by stellar feedback, and therefore requiring confinement by external pressure to prevent them from dispersing, as in the interpretation by Field et al. (2011) of the H09 sample. However, if we adopt the interpretation that star-forming GMCs are undergoing global and hierarchical collapse, pressure confinement is not satisfactory, since in this scenario the clumps should be gravitationally-dominated as well. Investigating the origin of these kinetic energy excesses within the scenario of collapsing clouds is one of the goals of this paper.

1.3. This work

In this work we create an ensemble of clumps in simulations of the formation and evolution of molecular clouds, in order to investigate their energy balance under a scenario of initial turbulence and subsequent gravitational collapse. Our simulations, of course, have a number of limitations, which are discussed in more detail in Sec. 4.1, but here we note that they neglect magnetic fields, stellar feedback, and have relatively low masses that restrict the clumps and cores we obtain to values typical of low-mass star-forming regions, which form low-mass stellar groups or low-mass clusters. Nevertheless, we expect that the results we obtain can be extrapolated to regions of larger masses.

The organization of the paper is as follows. In Sec. 2.1 we briefly describe the simulations, and in Sec. 2.2, we describe the clump-finding algorithm used to define clumps at various values of volume density, $n_{\rm th}$, as well as the selection criteria we used in order to avoid considering unrealistic clumps (i.e. those that would be affected by stellar feedback in reality). Next, in Sec. 3, we present our results on the energetics of the clumps and cores and their implications on Larson's relations. In Sec. 4 we discuss our work in context with recent related numerical studies, as well as the range of applicability, possible extrapolations, and limitations of our study. Finally, in Sec. 5 we present a summary and some conclusions.

2. Numerical data and analysis

2.1. The simulations

The simulations used in this work are those presented in Gómez & Vázquez-Semadeni (2014) and Heiner et al. (2015). For historical reasons, in this paper we will refer to these simulations as RUN20 and RUN03, respectively. Both simulations were performed with the code Gadget-2 (Springel et al. 2001), using $296^3 \approx 2.6 \times 10^7$ SPH particles and a numerical box of 256 pc per side. Each SPH particle is characterized by a single mass and a smoothing length, the latter defined as the radius of the volume that con-

tains 40 ± 5 neighboring particles. The simulations include the prescription for the formation of sink particles by Jappsen et al. (2005), and the fix proposed by Abel (2011), which eliminates several unphysical effects that arise in the standard SPH prescription, and describes more accurately a number of physical instabilities, such as the Kelvin-Helmholz and Rayleigh-Taylor instabilities. Both simulations used the cooling and heating functions of Koyama & Inutsuka (2002), corrected for typographical errors as described in Vázquez-Semadeni et al. (2007).

In RUN20, the (uniform) initial density and temperature were set at $1\,\mathrm{cm}^{-3}$ and 5206 K, and the mass per SPH particle is $\approx 0.02\ M_\odot$ so that the total mass in the box is $5.26 \times 10^5 M_\odot$. In this simulation, two cylindrical streams of warm neutral atomic gas, of diameter 64 pc and length 112 pc, were set to collide at the central ($x = 0$) plane. In addition, a small amount of turbulent energy was added (with speeds $\sim 10\%$ of the collision speed), at wave numbers $k = 8\text{-}16 \times 2\pi/L$, where L is the box size, so that the perturbations are applied at scales smaller than the inflow diameter. The collision produces a turbulent cloud, which grows in mass until it becomes gravitationally unstable and begins to collapse (e.g., Vázquez-Semadeni et al. 2007; Heitsch & Hartmann 2008). The collapse, however, is irregular and chaotic, because of the turbulence in the cloud, which creates a multi-scale and multi-site chaotic collapse (Heitsch et al. 2008; Vázquez-Semadeni et al. 2009), rather than a monolithic one, producing a complex morphology, in which filamentary structures arise self-consistently. We refer the reader to Gómez & Vázquez-Semadeni (2014) for more details.

On the other hand, RUN03 was produced with the aim of avoiding the over-idealized conditions of a colliding-flow simulation, in which the flows are perfect cylinders with circular cross-sections, moving in opposite directions along the same axis. Instead, RUN03 was started by applying a Fourier turbulence driver with purely solenoidal modes, with wave numbers in the range $1 < kL/2\pi < 4$ over the first 0.65 Myr of the simulation, reaching a maximum velocity dispersion of $\sigma \approx 18$ km s^{-1}. This produces a complex network of sheets and filaments, which subsequently grow by gravitational accretion. In this simulation, the initial density and temperature were set at 3 cm^{-3} and 730 K, respectively, the total mass in the box was $1.58 \times 10^6 M_\odot$, and the mass per SPH particle was $\approx 0.06\ M_\odot$.

	t (Myr)	σ_v (km/s)	M$_{sink}$ (M$_\odot$)	SFE
RUN03	15.6	4.15	83.8	0.0002
	18.2	3.69	512.9	0.0012
	18.5	3.65	576.9	0.0013
	19.5	3.50	1300.0	0.0027
	22.1	3.21	6786.9	0.1200
RUN20	20.8	0.536	57.0	0.0032
	21.1	0.533	119.6	0.0067
	22.2	0.526	763.5	0.0409
	24.8	0.518	2995.7	0.1471
	26.5	0.517	4817.1	0.2234

Table 2: Total velocity dispersion, mass in sinks, and total SFE ($= M_*/(M_* + M_{\rm cold})$) at the times analyzed in the two simulations. Here, $M_{\rm cold}$ is the total mass in cold gas ($n > 50$ cm^{-3}).

Finally, in both simulations, the density threshold to form sink particles is set at 3.2×10^6 cm^{-3}, and no prescription for feedback is included. This implies that we must be careful in the choice of the clumps to be analyzed, in order to avoid including clumps that would have already been destroyed by stellar feedback, had it been included (see Sec. 2.2). The main parameters of the simulations are summarized in Table 1.

In these simulations, we analyze the physical properties of the clumps formed self-consistently, using a clump finding algorithm that we describe in Sec. 2.2. We then measure the mass, size, density and velocity dispersion of the clumps in physical space (not projected), to investigate their energy balance. Table 2 gives the velocity dispersion, mass in sinks and global star formation efficiency, SFE $= M_*/(M_* + M_{\rm cold})$, of the simulations at the chosen times. Here, $M_{\rm cold}$ is the total mass in cold gas ($n > 50$ cm^{-3}, T$\sim$10-20 K).

2.2. Generation of the clump ensemble

In the present work, we use the term "clump" in a loose way, simply to denote a local density enhancement above a given density threshold, except for the objects defined at the highest thresholds ($n_{\rm th} \geq 10^5$ cm^{-3}), which will be referred to as "cores", and those defined at the lowest thresholds ($n_{\rm th} = 300$ cm^{-3}), which will be sometimes referred to as "clouds". No impli-

	L [pc]	T_0[K]	n_0[cm^{-3}]	$m_{\rm sph}$ [$M_\odot$]	M$_{\rm box}$ [$M_\odot$]	Type
RUN03	256	730	3	0.06	1.5×10^6	Decaying turbulence
RUN20	256	5206	1	0.02	5×10^5	Colliding flows

Table 1: Initial conditions in simulations. L is the box size, $m_{\rm sph}$ is the mass per SPH particle, T_0 is the initial temperature, and n_0 is the initial density.

cation is made about a specific density or mass range for the clumps, nor about whether they will form only a few stars, or a cluster. This is a somewhat looser usage of the term "clump" than the meaning adopted sometimes, of clumps being the gaseous objects from which stellar clusters form (see, e.g., the review by Blitz & Williams 1999). However, for the purposes of the present study, which considers objects with a variety of densities and masses, our more generic terminology is adequate. Note that, in general, a single clump at a lower threshold may contain several clumps at a higher one.

In what follows, we first describe the procedure for finding the clumps, and then the selection criteria to include them in our sample.

2.2.1. Clump finding algorithm

The procedure to find clumps in the simulation was performed directly in the SPH particles, without a previous mapping onto a grid. This allows the procedure to find the clumps in a manner independent of the grid resolution and without the smoothing inherent to the gridding procedure.

The procedure is the following. First, we select all the SPH particles in the simulation with density above a certain threshold, n_{th}. We then locate the particle with the highest density. This particle and all those located within its smoothing length are labeled as members of the clump. Then, the following steps are iterated: we locate the member of the clump with the highest density to which this subprocedure has not been applied, and then label as members all the particles within a smoothing length not-yet belonging to the clump. The iteration ends when all the clump members are examined. If there are particles remaining with density $n > n_{th}$ that are not yet members of any clump, we locate the one with the highest density and use it to define a new clump and the procedure is repeated.

In summary, this procedure finds the largest connected object above a volume density threshold.

2.2.2. Clump sample

For the analysis of both simulations we only considered clumps with more than 80 SPH particles ($M \geq 4.8\ M_\odot$ in RUN03 and $M \geq 1.6\ M_\odot$ in RUN20), in order to guarantee that they are well resolved, according to the criterion by Bate & Burkert (1997). This amounts to twice the number of particles contained within one particle smoothing length.

Since in RUN03 we first apply a turbulent driver, and then we leave the simulation to decay and collapse, we analyze various timesteps that correspond to different levels of the turbulence and different evolutionary stages of the clouds and clump populations. Specifically, we analyze the simulation at t = 15.6, 18.1, 18.5, 19.5, and 22.1 Myr. Sink ("star") formation begins in the simulation at $t \sim 14.7$ Myr, and at $t = 22.1$ the total mass in sinks is $6787 M_\odot$, amounting to $\sim 0.4\%$ of the total mass in the box, and $\sim 4\%$ of the cold gas mass. At these times, we generate an ensemble of clouds, clumps and cores by applying the clump-finding algorithm at the density thresholds, $n_{\rm th}$ = 300, 10^3, 3×10^3, 10^4 and 10^5 cm^{-3}, for both simulations.

In RUN20 the turbulence in the cloud develops self-consistently, and so it never is excessive (i.e., not larger than what would be produced self-consistently by the gravitational contraction). Nevertheless, the structures (filaments and clumps) still evolve, the filaments gathering mass by accretion from their surrounding medium, and the filaments themselves feeding the clumps inside them (Gómez & Vázquez-Semadeni 2014). However, close inspection of the evolution of the filament/clump systems shows that they form at about the same time, and the flow along the

filaments toward the clumps develops later (see also Gong & Ostriker 2015). This will be relevant later in the investigation of whether the accretion from the filaments onto the clumps has any effects on the dynamics of the latter (Sec. 3.2.3). In this simulation we choose timesteps that exhibit well-defined filament/clump systems, in order to study whether clumps accreting from filaments exhibit systematically larger velocity dispersions than those expected from energy equipartition considering the mass of the clump only. Specifically, we consider time steps at t = 20.8, 21.2, 23.2, 24.8 and 26.5 Myr.

In order to find cores of high column density we selected some timesteps [3], t = 18.1 and 18.5 Myr for RUN03, and t = 20.8 and 21.2 Myr for RUN20, and we applied the clump-finding algorithm at $n_{\rm th}$ =3x10^5 and 10^6.

In the SPH simulations used in this work, the SPH particle mass ($m_{\rm SPH}$; see Table 1) is fixed. Thus, for clumps satisfying the above conditions, we compute the gas mass as $M_{\rm gas} = N_{\rm cl} m_{\rm SPH}$, where $N_{\rm cl}$ is the number of SPH particles contained in the clump. Note that , in general, the measured masses are smaller at higher thresholds, because denser objects are embedded within larger ones that are more massive, but less dense on average.

Finally, note also that the clumps exhibit complex morphologies, being far from spherical in general, and often display elongated and twisting shapes, as shown in Fig. 1. This implies that there is an inherent ambiguity in the definition of the clump size, since in general they have more than one characteristic dimension. With this caveat in mind, we compute the clump "radius" as $R = (3V/4\pi)^{1/3}$, where V is the sum of the specific volumes of all particles that belong to a clump, i.e.,

$$V = \sum_{i=1}^{N_{\rm cl}} V_i = \sum_{i=1}^{N_{\rm cl}} \frac{m_{\rm sph}}{\rho_i} = m_{\rm sph} \sum_{i=1}^{N_{\rm cl}} \rho_i^{-1}, \qquad (5)$$

where ρ_i is the density of particle i. With this definition, the mean density of the clump ($\bar{\rho} = M/V$) is given by,

$$\bar{\rho} = \frac{m_{\rm sph} N_{\rm cl}}{m_{\rm sph} \sum_{i=1}^{N_{\rm cl}} \rho_i^{-1}} = \frac{N_{\rm cl}}{\sum_{i=1}^{N_{\rm cl}} \rho_i^{-1}}. \qquad (6)$$

Since feedback is not included in either of our simulations, we need to apply some kind of criterion to avoid including clumps that exhibit unrealistic physical properties because feedback should be already dominating their dynamics if it had been included. We therefore consider only clumps that, at a density threshold of $n_{\rm th} = 10^5$ cm^{-3}, have a star formation efficiency SFE$_5$ < 65%, where the SFE$_5$ is defined as

$$\mathrm{SFE}_5 = \frac{M_*}{M_{\rm tot,5}}, \qquad (7)$$

and $M_{\rm tot} = M_* + M_{\rm gas,5}$, M_* is the mass in stars (sink particles) and $M_{\rm gas,5}$ is the mass in dense gas above $n = 10^5$ cm^{-3}. We choose this value as a compromise between realistic SFEs for massive cluster-forming clumps (10–50%, Matzner & McKee 2000; Lada & Lada 2003) and obtaining a reasonably large statistical clump sample.

For lower clump-defining density thresholds, we must impose a further restriction on the maximum accepted SFE at each threshold. Star formation is a highly spatially intermittent phenomenon, so that star-forming sites only occur at a few and highly localized positions that have the highest densities in a large MC. Thus, if one focuses on a given star-forming site and measures the gas mass around it at various thresholds, this mass will be larger for lower thresholds, since this procedure includes progressively more material from progressively larger distances from the star-forming site. In consequence, the measured SFE around a star-forming site will be smaller at lower thresholds (as long as no other site enters the domain defined by the threshold). This is consistent with the general trend that lower-density objects generally are observed to have lower SFEs (e.g., Palau et al. 2013; Louvet et al. 2014).

[3] It is important to note that the original timestep between successive dumps in both simulations was $\Delta t = 0.136$ Myr. This timestep proved inadequate to resolve the formation and collapse of the densest clumps which, at $n > 10^6$ cm^{-3}, have free-fall times $\tau_{\rm ff} \lesssim 0.045$ Myr. Therefore, to find cores of high column density we restarted the simulations shortly before new sinks appeared with 10 times finer temporal resolution.

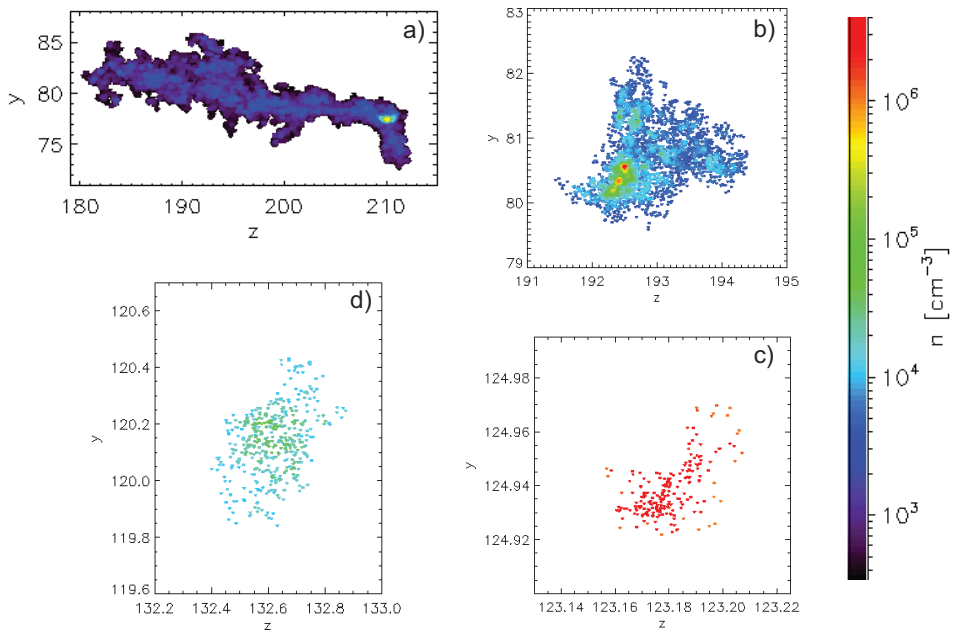

Fig. 1.— Clumps at different density thresholds and snapshots in both simulations at the same density scale. a) Clump in RUN03 at $n_{th} = 300\ n_0$; b) RUN20, $n_{th} = 10^3\ n_0$; c) RUN03, $n_{th} = 3 \times 10^3\ n_0$; d) RUN20 $n_{th} = 10^4\ n_0$. We find, in general, more elongated structures than spherical.

To replicate this trend, we require progressively smaller efficiencies at lower thresholds in order to admit a clump in our sample. Thus, the maximum star formation efficiency, $\mathrm{SFE}_{\mathrm{max},i}$, for any clump included in our sample at threshold i is given by

$$\mathrm{SFE}_{\mathrm{max},i} = \left(\frac{M_5}{M_i}\right) \mathrm{SFE}_5, \qquad (8)$$

where M_5 is the total mass in clumps defined at threshold $n_{\mathrm{th}} = 10^5$ cm^{-3}, M_i the total mass in clumps defined at the i-th threshold, $n_{\mathrm{th},i}$, and $\mathrm{SFE}_5 = 65\%$. Figure 2 shows the mass fraction M_5/M_i as a function of $n_{\mathrm{th},i}$ for the two simulations. With this prescription, we avoid including clumps whose measured SFEs at low thresholds are so large that at a higher threshold they would exceed the maximum SFE allowed for it.

3. Results

3.1. Testing for Larson's relations

3.1.1. The density-size relation

We first check whether our clump sample, occurring in clouds undergoing global collapse, satisfies Larson-like relations. Figure 3 shows our clumps in the n *vs.* L and σ_{v} *vs.* L diagrams for the two simulations. In this plot, the different colors represent different column densities, the dashed lines represent various column densities, and the symbols correspond to the volume density thresholds used to define the clumps.

Due to the resolution requirement that our clumps contain at least 80 SPH particles, our sample is mass-limited from below, so that the clumps are constrained to have masses $M_{\mathrm{cl}} \geq 1.6\,M_\odot$ in RUN20 and $M_{\mathrm{cl}} \geq 4.8\,M_\odot$ in RUN03.

A first point to notice in Fig. 3 is that RUN03 produces more clumps than RUN20. This is because in RUN03 the density structures are scat-

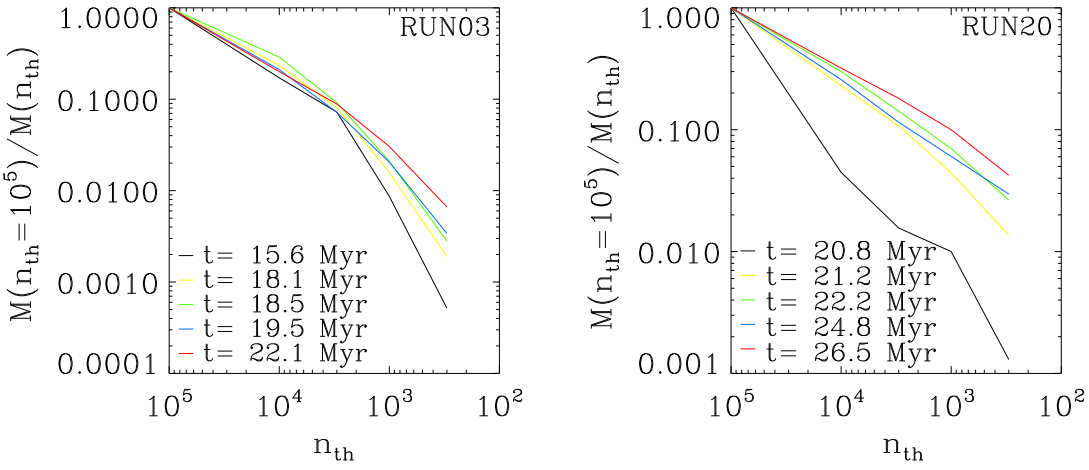

Fig. 2.— Maximum SFE ($SFE_{max,i}$) allowed for clumps included in the sample as a function of density threshold, $n_{\rm th}$, as given by eq. (8), at the various timesteps considered in the two simulations.

tered throughout the simulation domain, since the clouds and clumps have been produced from a large number of turbulent fluctuations in the early stages of the run. Instead, in RUN20 there is only a single large cloud complex, produced initially by the collision of the large cylindrical WNM streams.

From Fig. 3, we also see that our clump sample does not follow the standard Larson $n \propto R^{-1}$ relation (Fig. 3). Instead, the entire sample occupies a triangular region in the n-R diagram, so that no single density-size relation exists. Additionally, we observe a very well defined group of points at nearly constant density for each volume density threshold. However, we also observe that, when the clumps are classified by column density (with various column density ranges shown as the different colors in the figure), then each sub-sample traces a slope R^{-1} as in the Larson (1981) density-size relation. This supports the notion that the density-size relation is an artifact of defining clumps by a column density threshold.

The fact that the clumps defined at a certain volume density threshold appear to have a nearly constant *volume* density was already noticed in numerical simulations by Vázquez-Semadeni et al. (1997) and Ballesteros-Paredes & Mac Low (2002), and later interpreted by Ballesteros-Paredes et al. (2012) and Beaumont et al. (2012) as a consequence of the steep slope of the high-density side of the density PDF, which implies that most of the volume (and even the mass) is at the lowest densities allowed by the threshold, if the threshold is above the density corresponding to the maximum of the PDF. The same is expected to happen for the column density, if it is also described by a lognormal or a power law with a slope steeper than -1 (Ballesteros-Paredes et al. 2012), again reinforcing the notion that the apparent constant column density of molecular clouds is an artifact of the restricted column density range allowed by the tracers used to observe them, such as the ^{12}CO line.[4]

An expression equivalent to Larson's density-size is that of mass *vs.* size, which reads $M \propto R^2$. Figure 4 shows the scaling of size *vs.* mass (left

[4] It has been argued by Lombardi et al. (2010) that the constant column density of molecular clouds is an actual physical property of molecular clouds, which can be observed in dust extinction maps that allow thresholds significantly lower than that claimed for the physical column density of the molecular clouds. However, the result by Ballesteros-Paredes et al. (2012) that the observed most common column density for a cloud is dominated by the lowest densities present in the cloud when the PDF slope is < -1 and by the highest densities otherwise can explain the result by Lombardi et al. (2010), if the bimodal pdf of the Galactic gas is taken into account (e.g., Vázquez-Semadeni et al. 2000b; Audit & Hennebelle 2005; Gazol et al. 2005). We plan to address this issue in a separate contribution.

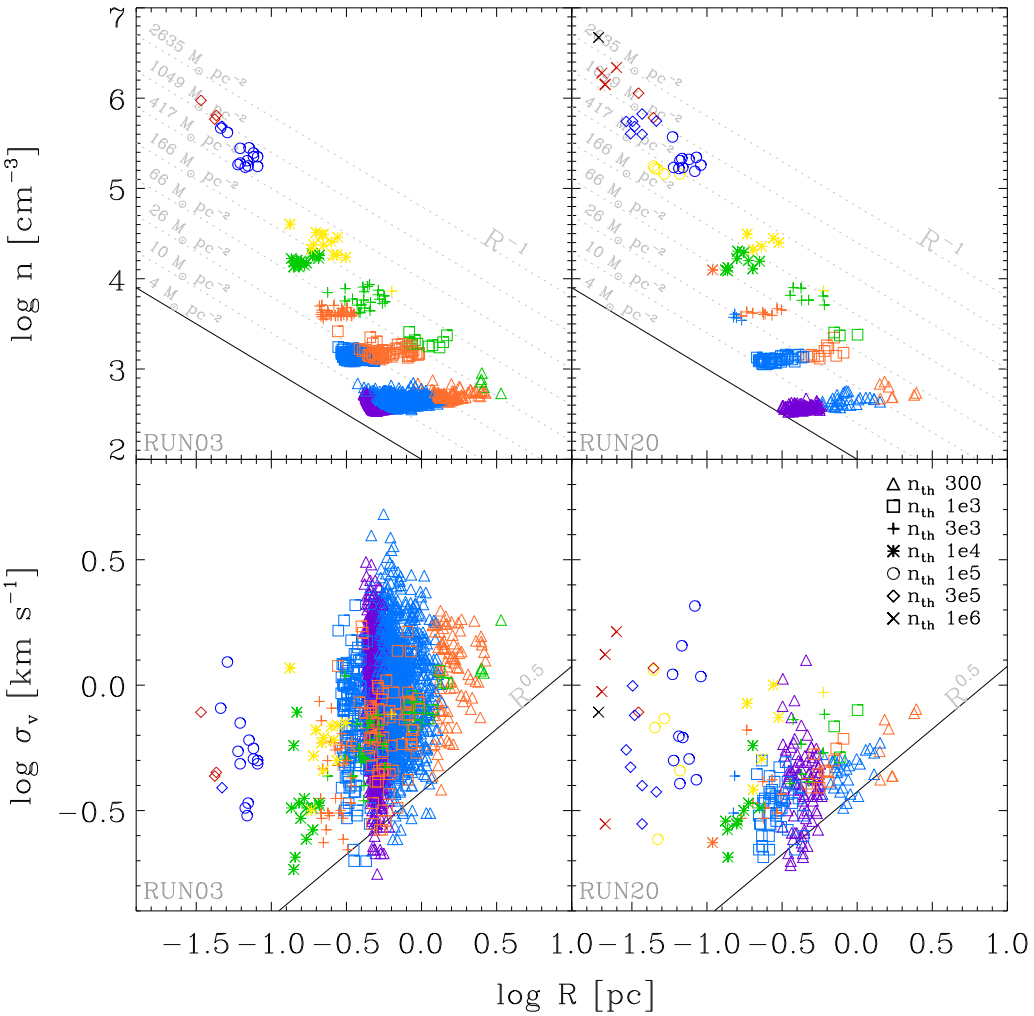

Fig. 3.— Larson-like relations for simulated clumps and cores. Symbols correspond to the volume density threshold used to define clumps. The dotted lines correspond to constant column density values and colors represent the different column density-ranges, bounded by the values of the dotted lines. Purple: $\Sigma < 10 M_\odot \mathrm{pc}^{-2}$; blue: $10 < \Sigma < 26 M_\odot \mathrm{pc}^{-2}$; orange: $26 < \Sigma < 66 M_\odot \mathrm{pc}^{-2}$; green: $66 < \Sigma < 166 M_\odot \mathrm{pc}^{-2}$; yellow: $166 < \Sigma < 417 M_\odot \mathrm{pc}^{-2}$; blue: $417 < \Sigma < 1049 M_\odot \mathrm{pc}^{-2}$; red: $1049 < \Sigma < 2635 M_\odot \mathrm{pc}^{-2}$, and black: $\Sigma > 2635 M_\odot \mathrm{pc}^{-2}$. Note that, by selecting clumps by column density, each sample follows a Larson-like density-size relation.

panels) and also the column density *vs.* mass (right panel) for our clump sample in the same Σ ranges as in Fig. 3. Solid lines correspond to $M \propto R^2$ (or constant-Σ). Again, it can be seen that, in both simulations, when the entire sample is considered, the clumps do not show constant column density (right panels, Fig. 4) nor an $M \propto R^2$ scaling (left panels, Fig.4). However, such a correlation reappears when the data are classified by column density. On the other hand, at every volume density threshold (different symbols for each threshold) clumps show the relation $R \propto M^{1/3}$, denoted by the dashed black line in Fig. 4, which is the scaling expected for clumps of constant

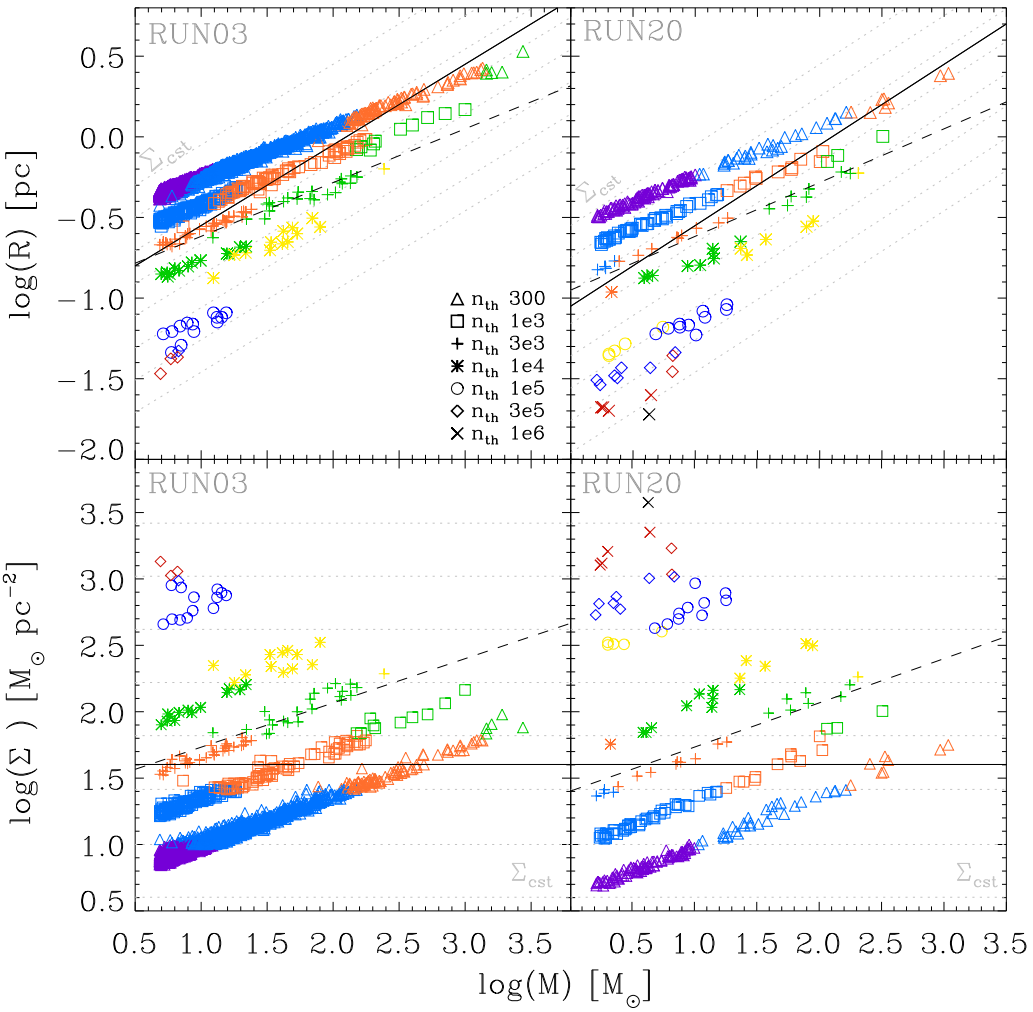

Fig. 4.— Size and column density *vs.* mass. The solid lines show the scaling implied by the density-size Larson-like relation; the dashed lines show the slope 1/3 corresponding to constant volume density. The color scheme, the symbols and the values of Σ (dashed gray lines) are the same used in Fig. 3. Note that the clumps belonging to a given Σ range follow a scaling similar to that implied by Larson's density-size relation.

volume density (Ballesteros-Paredes et al. 2012; Beaumont et al. 2012).

It is worth noting in the *right* panels of Fig. 4 that clumps in a given range of column densities include clumps defined at various *volume* density thresholds. Nevertheless, there is a net trend for clumps defined at higher volume density thresholds to fall in higher column density ranges. This behavior is also present in observational data (see, e.g., Figure 14 of Barnes et al. 2011).

3.1.2. The linewidth-size relation

With respect to the σ_v-R relation, we notice in Fig. 3 that the $\sigma_v \propto R^{1/2}$ scaling is not satisfied by the whole clump sample in either of the simulations and, instead, the ensemble of clumps fills a large area in the σ_v-R diagram (as is often the case in observational surveys as well; see, e.g.,

Heyer et al. 2001; Ballesteros-Paredes et al. 2011; Heyer & Dame 2015, and references therein). However, it can be observed that the clumps with $\log(R/\mathrm{pc}) \gtrsim 0.5$ are bounded from below by approximately the Larson slope (right panels of Fig. 3). A similar effect was observed by Vázquez-Semadeni et al. (1997). In addition, it is also noticeable that some of the samples at certain Σ ranges (see, for example the orange and green points) seem to follow this scaling. In Sec. (3.2.4) we discuss the origin of the observed scatter.

3.2. Generalization of Larson's relations and energy balance

3.2.1. The KH diagram

The results from the previous section show that the clumps defined by volume density thresholds in the clouds in our simulations of global, hierarchical gravitational collapse do not seem to follow the linewidth-size relation. Instead, Larson-like density-size (and equivalent) relations appear when the selection of the clumps is done by means of a *column* density threshold or range. Larson-Like linewidth-size relations appear for *some* of the clumps.

We now test whether our clump sample follows a relation of the form of eqs. (3) or (4); i.e., we test for whether the clouds appear to be near virial equilibrium or energy equipartition, respectively, where the latter is consistent with free-fall. These relations can be considered as the generalization of Larson's relations when the column density of the objects in the sample is not constant.

Figure 5 shows the ratio $\sigma/R^{1/2}$ *vs.* Σ for clumps in RUN03 and RUN20. In what follows, we refer to this diagram as the Keto-Heyer (or KH) diagram (Keto & Myers 1986, H09). The solid line corresponds to virial equilibrium and the dashed line corresponds to energy equipartition, or free-fall condition. Contrary to figures 3 and 4, in these plots we use colors to denote the volume density thresholds at which clumps were defined, and different symbols to represent the timesteps considered in each simulation. Column density has been computed as $\Sigma = M_g/\pi R^2$ where M_g represents the gas mass in the clump (we will consider the stellar mass—i.e. sink mass, M_*—later).

3.2.2. Low-column density clumps

The first noticeable feature in these plots is the group of clumps at the lowest volume density threshold, i.e. $n_{\mathrm{th}} = 300 n_0$ (yellow symbols), which also have the lowest surface densities. These clumps are seen to occupy a region in the diagram that extends from the virial and free-fall lines to over one order of magnitude in $\sigma_{\mathrm{v}}/R^{1/2}$ above those lines, at roughly constant column density. We note that this is precisely the kind of behavior displayed in observational clump surveys (see, e.g., Figure 10 of Keto & Myers (1986) and Figure 13 of Leroy et al. (2015)).

Another frequent way of displaying the energy balance of the clumps is by plotting the "virial parameter" $\alpha = 2E_{\mathrm{k}}/|E_{\mathrm{g}}| = 5\sigma_{\mathrm{v}}R/GM$ (Bertoldi & McKee 1992). Figure 6 shows this parameter versus the clump mass for the two simulations. As in Fig. 3, the clumps with the lowest masses exhibit the largest scatter in α, with excesses of up to nearly two orders of magnitude. Again, this is similar to the observed behavior of clump surveys (see, e.g., figure 16 of Barnes et al. 2011).

This behavior is generally interpreted as implying that these clouds have an excess of kinetic energy over their gravitational energy, therefore being unbound, and needing to be confined by an external pressure to avoid rapid dispersal or else that they are being dispersed by the energizing action of stellar feedback. This latter possibility is not possible in our simulations, because we have not included any kind of stellar feedback, with the purpose of examining the action of only the initial assembling turbulent motions and of the gravitationally-driven motions.

An alternative possibility is that, if turbulent compressions in the atomic interstellar medium (ISM) are causing the early assembly stages of these clouds, their associated velocities may be larger than the corresponding gravitational velocities for those objects, although in this case their role is to *assemble* the clouds rather than to disperse them, in the context of *converging flows* from large-scale turbulent fluctuations. Later, as a cloud gains mass, its gravitational velocity may begin to dominate over the initial turbulent compression that started it, which may itself tend to dissipate.

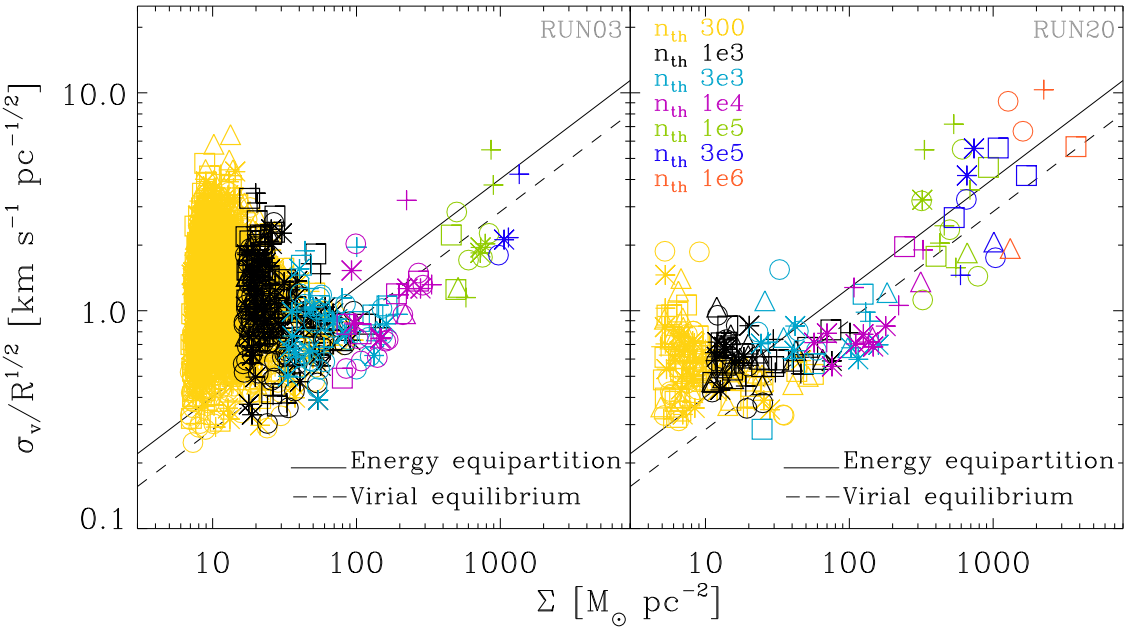

Fig. 5.— Generalization of Larson's scaling relations. The clouds at $n_{\rm th} = 300 n_0$ can be considered as atomic because of their low column density. Here, colors represent the different volume density thresholds used to define clumps with the clump-find algorithm described in section 2.2. Symbols represent different time-steps for RUN03 (△=15.6, □=18.1,+=18.5, ∗=19.5, ◯=22.1) and RUN20 (△=20.8, □=21.2,+=22.2, ∗=24.8, ◯=26.5).

To test for this, in the *top row* of Fig. 7 we show the clouds obtained at the lowest density threshold ($n_{\rm th} = 300$ cm^{-3}) in the KH diagram, but representing different mass ranges with different colors. Note that colors in these plots are also representative of sizes ranges, given that all these clumps have similar volume densities (cf. Sec. 3.1.1), and therefore the most massive ones are also the largest ones. The most massive clumps are seen to lie closest to the virial and equipartition lines, suggesting that these objects tend to be dominated by the gravitational velocity rather than by the turbulent velocity. This means that they have the largest gravitational velocities at a given column density, consistent with an evolutionary picture where the clumps are first assembled by large-scale turbulent compressions and, as they grow, they change from turbulent assembly to gravitational contraction.

This scenario can be further tested by measuring the mean velocity divergence in each clump [5], which shows whether the clump is contracting or expanding as a whole. A negative mean divergence means that the clump is contracting on average and, if its velocity is not driven by gravity, then its contraction must be a turbulent compression from the outside gas (e.g., Vázquez-Semadeni et al. 2008; González-Samaniego et al. 2014; Pan et al. 2015). The *bottom row* of Fig. 7 shows the histograms of the mean velocity divergence of all the clouds defined at the lowest threshold ($n_{\rm th} = 300$ cm^{-3}) and with masses $M < 100 M_\odot$ which are the clumps exhibiting the largest scatter in the KH diagram. We see that more than half of the clumps ($\sim 60\%$ in both simulations) have negative divergence, indicating that they are

[5]The particle velocity divergence was obtained directly from the GADGET-2 code, which computes the divergence in terms of the kernel function, the density and the velocity of each particle. Therefore, the errors in the velocity divergence are of the same order as those in the integration of the equations.

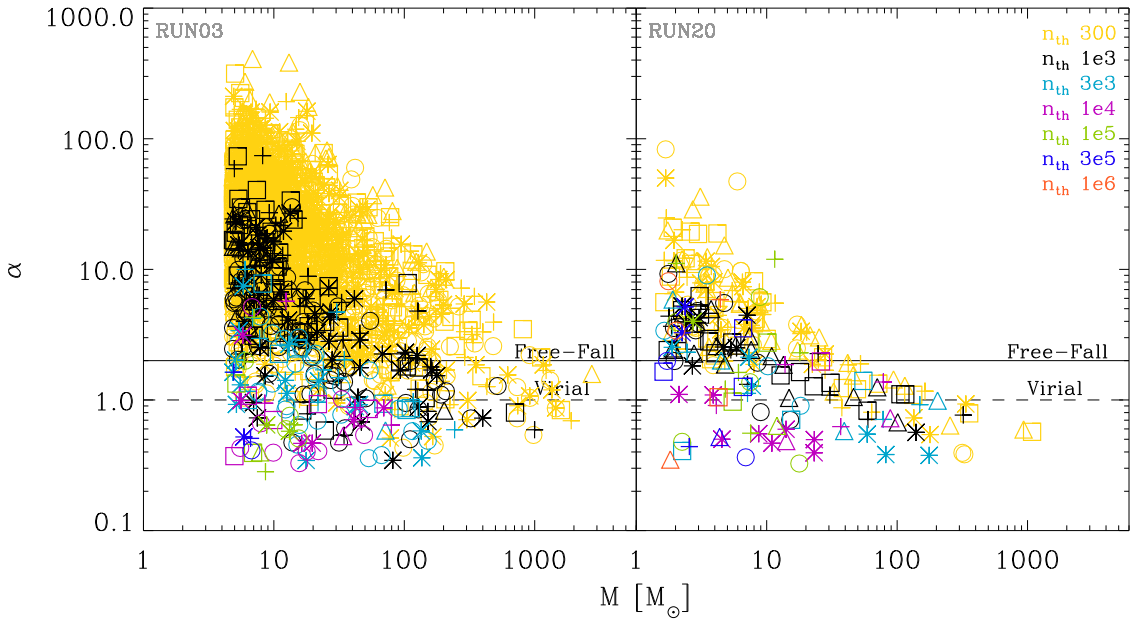

Fig. 6.— α parameter as a function of mass for the clumps for both simulations. Symbols represents different time steps, RUN03 (△=15.6, □=18.1,+=18.5, ∗=19.5, ◯=22.1) and RUN20 (△=20.8, □=21.2,+=22.2, ∗=24.8, ◯=26.5).

contracting on average, and therefore are in the process of *assembly*, although significant fraction is undeniably in the process of *dispersal*.

Figure 8 shows the velocity divergence histograms for all the SPH particles conforming some individual clumps, at similar masses (*top*: low-mass, *bottom*: intermediate-mass) and different values of the mean velocity divergence (*left*: negative, converging clumps; *right*: positive, dispersing clumps). From this figure, we note that the clumps, in general, contain a wide range of values of the divergence; quite wider, in fact, than the range of *average* divergences seen in Fig. 7, as expected for the distribution of partial averages of a random variable. In particular, even the clumps with negative mean divergence contain a substantial amount of particles where the local divergence is positive. Note, however, that a local positive divergence does not necessarily imply that the object is expanding globally. For example, a core undergoing non-homologous collapse, with an increasing infall velocity towards its center, will have a positive divergence in its envelope, because of the stretching caused by the differential infall speed. This in fact suggests that in fact our estimate of the fraction of contracting clumps based on the mean divergence may actually underestimate the actual fraction.

3.2.3. High-column density clumps

While in the previous section we have discussed the kinetic energy excess in low-column density clumps in the KH diagram, another feature in Fig. 5 is that some of the highest-column density objects also exhibit an excess of kinetic energy over the equipartition value, especially in the case of RUN20.

As mentioned in Sec. 1.2, clumps that appear significantly above (by factors of a few) the virial equilibrium line in the KH have often been interpreted as being gravitationally unbound, and requiring an external confining pressure to avoid being dispersed in a crossing time (e.g., Keto & Myers 1986; Field et al. 2011). However, it is also possible that the apparent kinetic energy excess is due to an underestimation of the relevant gravitational mass involved in the clump dynamics, as proposed, for example, by H09 for their

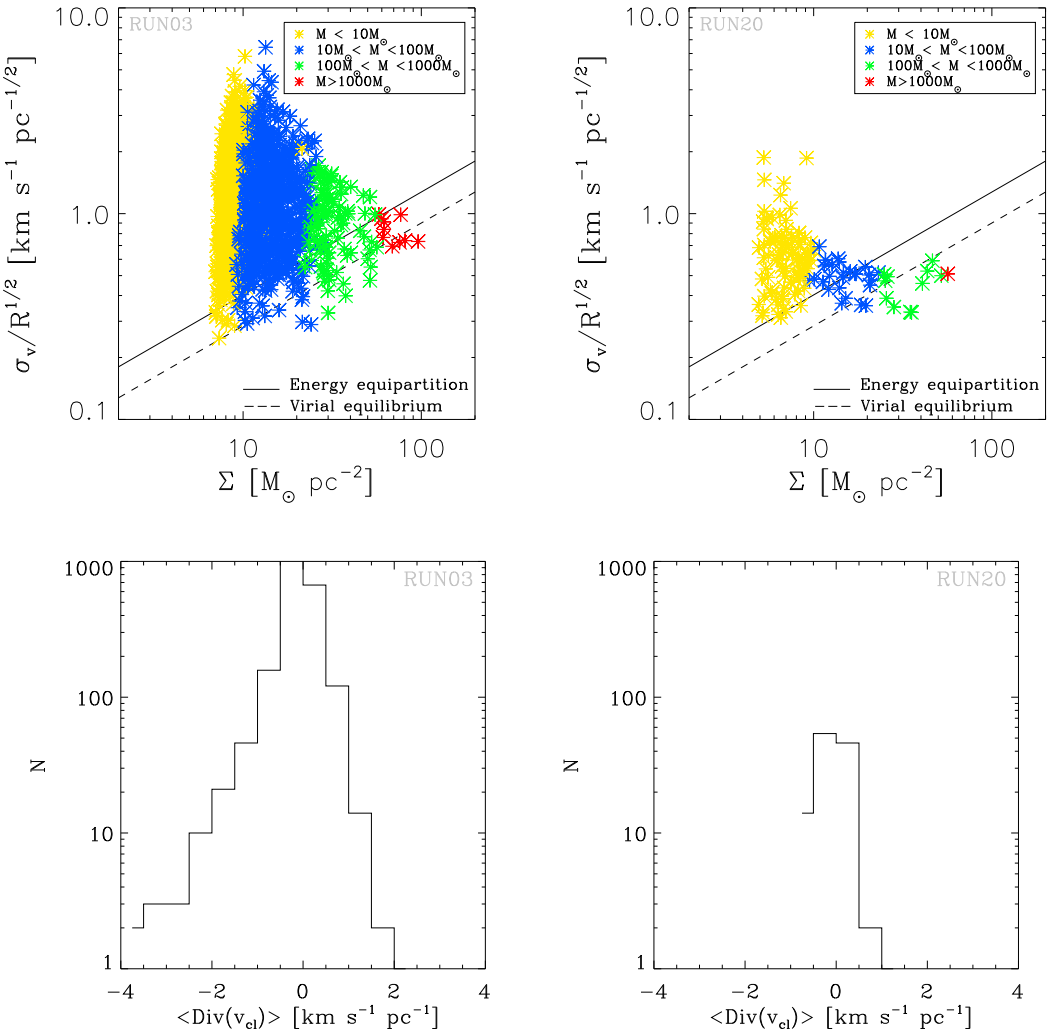

Fig. 7.— *Top:* Clumps defined at the lowest density threshold ($n_{\rm th} = 300\,{\rm cm}^{-3}$) plotted in the KH diagram. Clumps at the lowest volume density threshold generally have the lowest column densities as well. Different colors represent clumps in different mass ranges. The most massive clumps are seen to lie closest to the virial and equipartition lines. The *bottom* row shows the histograms of the mean velocity divergence in the clumps defined at $n_{\rm th} = 300$ cm^{-3} and with masses $M < 100 M_\odot$, in RUN03 (*left*) and in RUN20 (*right*).

MC sample. Two mechanisms that come to mind for providing additional mass beyond that directly measured in a clump are the mass in stars and the mass of external accreting material that is part of the same gravitational potential well. Even if our high-Σ clumps and cores do not show a very large excess in the $\sigma_{\rm v}/R^{1/2}$ ratio, we investigate their energetics under these two possibilities.

The "stellar mass effect"

One obvious source of mass in protostellar cores is the mass in (proto-)stellar objects which, in the case of cluster-forming clumps, may reach observed values of up to 30–50% (Lada & Lada 2003). We thus re-compute the location in the KH diagram of those cores and clumps that do contain sink particles, adding the mass of the lat-

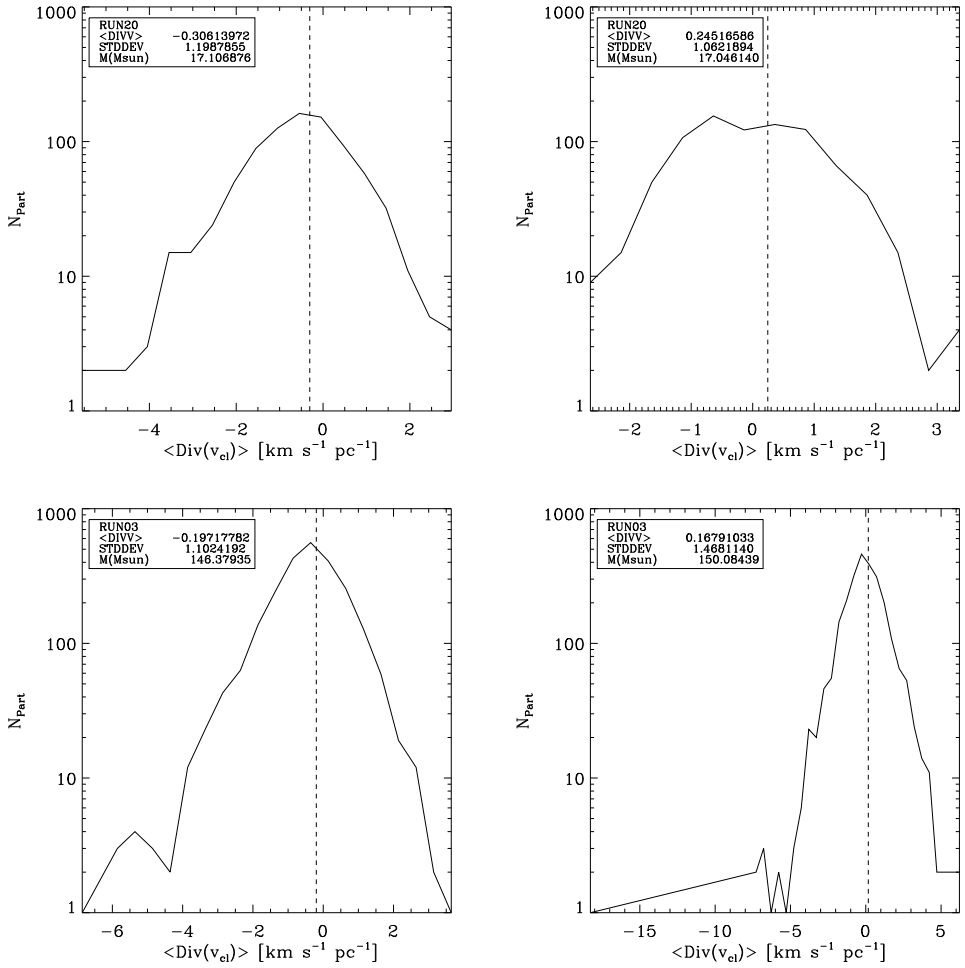

Fig. 8.— Histograms of the velocity divergence for all the SPH particles belonging to four representative low- to intermediate-mass individual clumps from both simulations. The *top* row shows clumps from RUN20, and the *bottom* row shows clumps from RUN03. The *left* colums shows clumps with negative mean divergence (i.e, converging on average), while the *right* column shows clumps with positive mean divergence (i.e., diverging on average).

ter to the computation of the core column density (i. e., now we consider $\Sigma = (M_g + M_{sink})/\pi R^2$). The result is shown in Fig. 9, where symbols represent the same timesteps as in Fig. 5 and clumps and cores that contain stellar particles are marked with a red diamond. From this figure, it is clear that the affected cores undergo a displacement in the KH diagram that relocates them closer to the virial equilibrium line in the case of RUN03, and to the region between the energy equipartition and virial equilibrium lines in RUN20. However, some cores with such an excess do not contain sinks, and for them, the excess cannot be explained by this correction.

The "filament effect"

A second possible mechanism for missing relevant gravitational mass in a core may be if the core is gravitationally accreting material from a surrounding structure, with the accretion driving turbulence into it (Klessen & Hennebelle 2010).

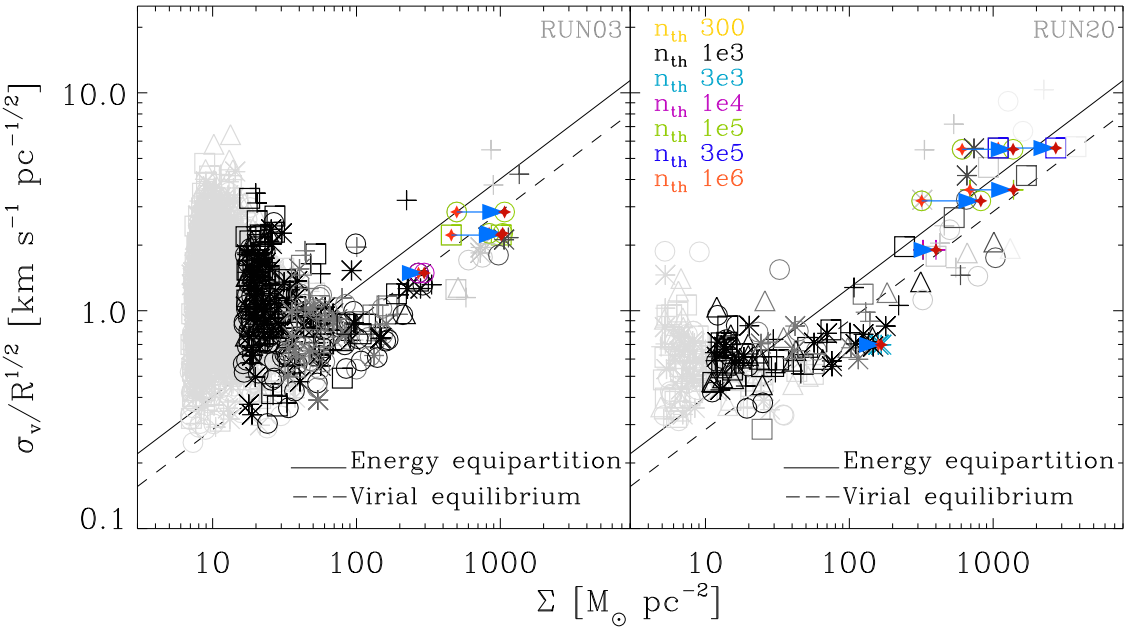

Fig. 9.— Correction to the location of sink-containing cores in the KH diagram (indicated by the arrows) due to the inclusion of the mass in sinks in the clumps' energy balance. The cores with sinks are denoted by a red diamond. As in figure 5, different symbols represent different times.

In particular, it has been found both in observations (e.g., Schneider et al. 2010; Kirk et al. 2013; Peretto et al. 2013) and numerical simulations (Gómez & Vázquez-Semadeni 2014), that filaments may provide an accretion channel of cloud material onto cores. In this case, it is reasonable to ask whether the velocity dispersion in the core reflects the gravitational potential of the entire filament/core system.

To test for this possibility, in both simulations we visually examined the set of dense cores in our sample exhibiting a kinetic energy excess, but not the "sink effect", to determine whether they belonged to a filament. Rather surprisingly, we found none. We thus reversed the procedure, visually searching for filament/core systems, and then analyzing their energy budgets.

Figure 10 shows one such filament/core system from RUN20 at $t = 26.5$ Myr at different density thresholds. The *right- bottom* corner of this figure shows this system on the KH diagram. Contrary to our expectation, this filament/core system exhibits a *lower* value of the ratio $\sigma_{\rm v}/R^{1/2}$ than that expected for a spherical configuration, appearing *below* both the equipartition and the virial-equilibrium lines in this figure. In hindsight, this is actually natural, since the gravitational potential of a filamentary object of length L is much lower than that of a spherical object of diameter L and the same volume density, implying that the velocity dispersion of the former should be significantly lower than that of the latter (Toalá et al. 2012; Pon et al. 2012).

However, it might still be possible that the central, roundish core, should have a larger velocity dispersion than that of an isolated core of the same dimensions and in equipartition, because of the accretion from the filament. Unfortunately, this system only appears roundish at $n_{\rm th} = 10^6$ cm^{-3}, and even at this threshold density, the core appears sub-virial. In fact, we had to relax our minimum-mass selection criterion (cf. Sec. 2.2.2) in order to include this core in the system, since it only contains 60 SPH particles, and it is therefore likely to be significantly affected by numerical dissipation. Thus, we cannot determine where it would be located in the KH diagram had it been free of numerical dissipation.

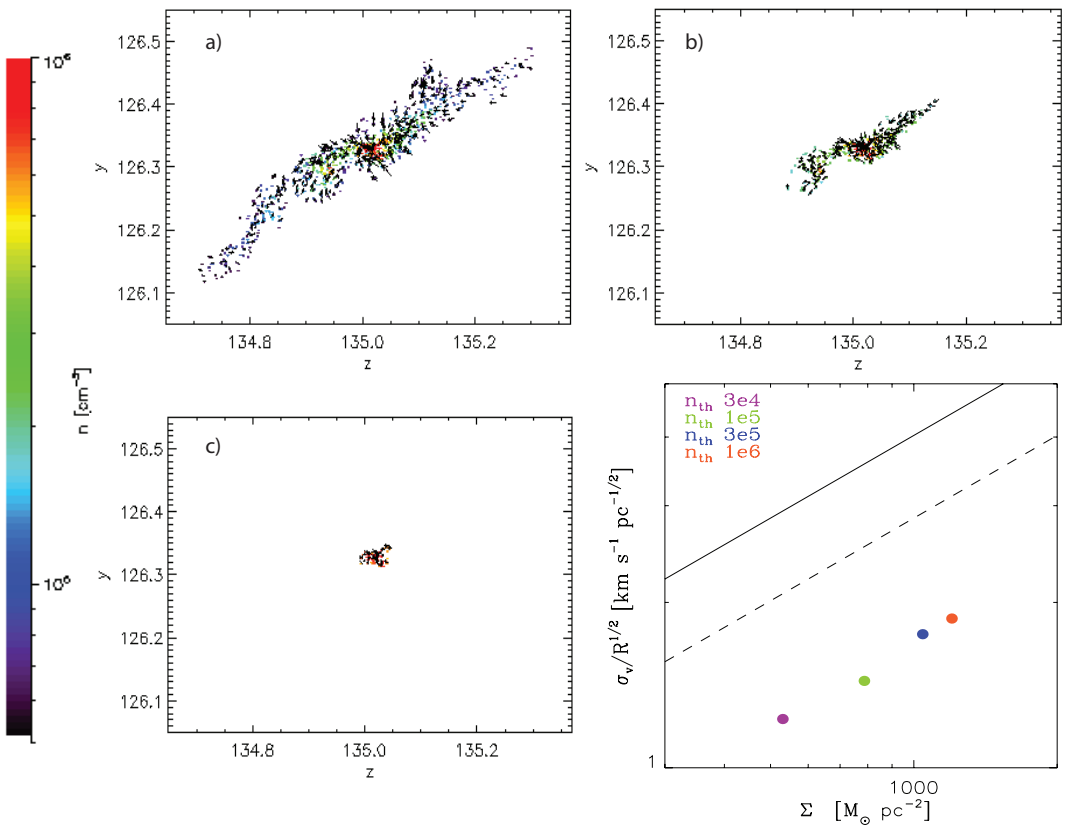

Fig. 10.— Filament/core system above a) $n_{\rm th} = 10^5$, b) 3×10^5 and c) 10^6 cm^{-3}. The right-bottom corner shows the filament/core system in the KH diagram at thresholds $n_{th} = 10^4$, 3×10^4, 10^5, and 10^6 cm^{-3}. The points corresponding to the various thresholds are seen to describe a line parallel to the equipartition and virial-equilibrium lines, but displaced to a lower value of the ratio $\sigma_{\rm v}/R^{1/2}$, except for the point corresponding to $n_{\rm th} = 10^6$ cm^{-3}, which is probably affected by numerical dissipation.

To try to answer this question, we searched for some other filament/core systems at larger scale, so that the central core would have a sufficient number of particles to be relatively free of numerical dissipation. However, we have been unable to accomplish this task, because of our restriction that the cores should have an SFE $< 65\%$ at $n_{\rm th} = 10^5$ cm^{-3}. Indeed, we found that all larger cores that appeared to be accreting from filaments already had efficiencies larger than this. This seems to be a consequence of the fact that the filaments and the cores grow roughly simultaneously, and accretion from the filament onto the core only begins by the time the core has already undergone significant sink formation, as also noted by Gong & Ostriker (2015). This suggests that cores located within filaments in their prestellar or early protostellar stages should not exhibit excess kinetic energies, because they are not accreting significantly from their filaments at these stages.

We conclude that filaments, and the pre- and protostellar cores located within them, tend to exhibit sub-virial velocity dispersions, due to the lower gravitational energies of these configurations than those of the spherical structures assumed for the virial velocity dispersion estimate.

Dispersing clumps and cores

After considering both corrections by the mass in sink particles and by existing in a filamentary envi-

ronment, we are nevertheless left with some dense cores whose kinetic energy excess cannot be explained by either of these effects. Such is the case, for example, of the cores indicated by the green and red '+' symbols with high values of $\sigma_{\rm v}/R^{1/2}$ in the right panel of Fig. 9. Figure 11 shows this core at a threshold $n_{\rm th} = 10^5$ cm^{-3} and at three times separated by 0.2 Myr, with the arrows indicating the velocity field on the plane shown. It can be seen that the core is actually being disrupted, and so this is indeed a case of a starless core that will probably never form stars.

3.2.4. Scatter propagation from KH to Larson

Figure 5 shows a considerable scatter, especially for low-Σ. In particular, it is clear that the scatter is reduced as Σ increases. We have interpreted this effect as a consequence of an increasing relative importance of self-gravity at increasing column density, except for those high-density objects that are being disrupted. Since we have argued that a Larson-like linewidth-size relation appears for objects near equipartition that are furthermore selected by near-constant column density, the scatter around equipartition should cause a scatter around the velocity dispersion-size relation as well. Indeed, a large scatter is also observed in the velocity dispersion-size plots for both runs (cf. Fig. 3)

To quantify this, we note that the scatter in the quantity $\mathcal{H} \equiv \sigma_{\rm v}/R^{1/2}$ is related to that in the velocity dispersion and in the radius by

$$d\ln\mathcal{H} = d\ln\sigma_{\rm v} - \frac{1}{2}d\ln R. \qquad (9)$$

The scatter $d\mathcal{H}$ around the equipartition value $(2\pi G\Sigma/5)^{1/2}$ (cf. eq. [4]) represents the (physical) deviation from equipartition for a given clump. Because the scatter $d\mathcal{H}$ merges the scatter in $\sigma_{\rm v}$ and in R, it is not possible to determine how $d\ln\mathcal{H}$ is distributed among $d\ln\sigma_{\rm v}$ and $d\ln R$. However, we can obtain an upper limit in the expected scatter in $\sigma_{\rm v}$ if we assume that it "absorbs" all of the scatter in $\mathcal{H}$, with none of it going to R; that is, assuming $d\ln\sigma_{\rm v} = d\ln\mathcal{H}$. In Fig. 12 we have plotted the error bars for $\sigma_{\rm v}$ in the velocity dispersion-size relation corresponding to the scatter in the $\mathcal{H}$ ratio from Fig. 5, for the three different column density ranges (represented with the color of the error bars, which are the same as in the plots of Fig. 3). It is clear from Fig. 12 that the scatter in the Larson-like velocity dispersion-size relation at low densities (purple points and error bar) is clearly contained within the estimated upper limit originating from the scatter in the KH diagram. Instead, for intermediate column densities (green points and error bar), for which there is still a large enough number of points to obtain good statistics and the scatter in the KH diagram is not large, we see that the upper limit to the scatter expected for $\sigma_{\rm v}$ is relatively small, and the points define a clear Larson-like linewidth-size relation. We conclude that the suggestion that clumps describe Larson-like relations when they are restricted to narrow column density ranges and they are close to energy equipartition is supported by our numerical clump sample.

4. Discussion

4.1. Limitations

As mentioned in Sec. 1.3, our numerical simulations have a number of limitations. In particular, our SPH simulations neglect all forms of stellar feedback and magnetic fields. We plan to perform a similar analysis in a future contribution including these physical agents, but our present study allows a first approximation to the problem. Furthermore, our chosen setups only produce objects similar to observed low-mass star-forming clumps and cores.

The neglect of stellar feedback has allowed us to investigate the energy budget of clumps due exclusively to the interaction of initial background turbulence and self-gravity, without complicating the velocity field with additional contributions from the feedback. Our study has shown that in this context, our simulated clump sample reproduces observed trends in the KH diagram. In our sample, gravity has an increasingly dominant role as the column density of the clumps increases. On the other hand, low-column density clumps are increasingly dominated by turbulence, although large-scale turbulent compressions are dominant in more than half of these objects, in which external turbulent compressions provide the initial "push" that triggers the assembly of the clumps. In these, gravitational contraction is expected to take over when the clump has grown sufficiently massive. The other half may actually correspond

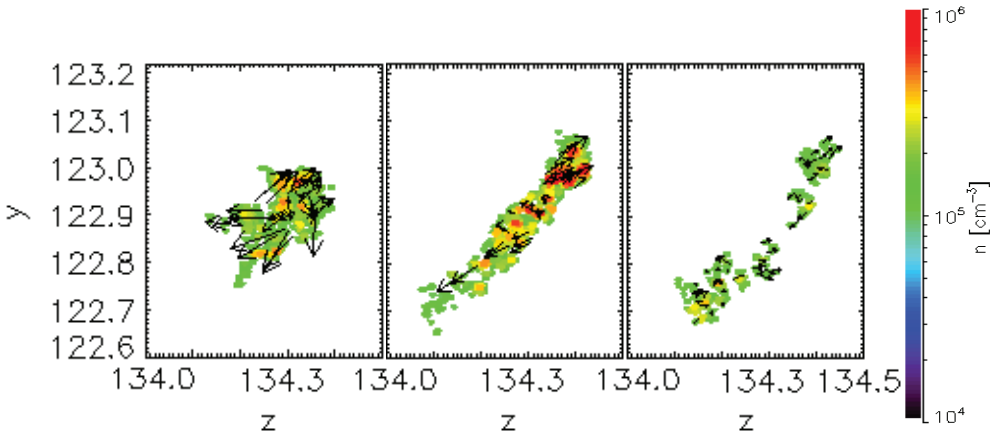

Fig. 11.— High-column density core from RUN20 at times $t = 22.2$, 22.4 and 22.6 (from left to rigth)Myr at $n_{th} = 10^5 \mathrm{cm}^{-3}$, showing that the core is being disrupted. The velocity field, shown by the arrows, also indicates that the clump is being dispersed, since it in general it is divergent.

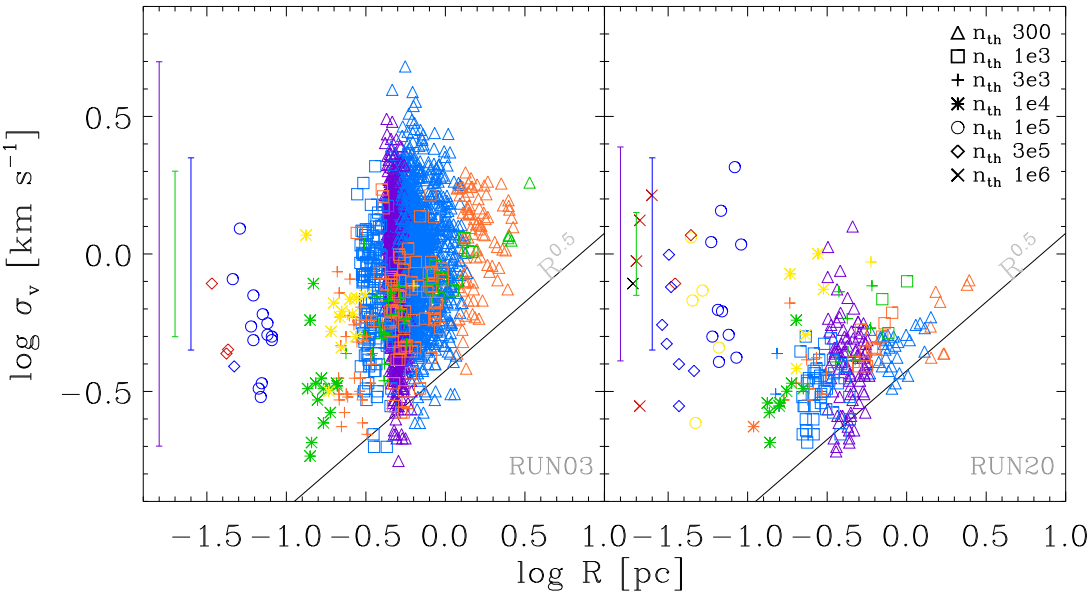

Fig. 12.— Larson velocity-size relation for clumps and cores in both simulations. Colors and symbols are the same as in Fig. 3. The error bars correspond to the scatter shown in Fig. 5, and their colors correspond to the Σ range.

to clumps that will not grow to high densities and masses.

Magnetic fields, on the other hand, even if insufficiently strong to support the clouds, as they are presently believed to generally be (e.g., Crutcher 2012), might possibly delay the collapses (Ostriker et al. 1999), or reduce the number or formation rate of collapsing objects (Vázquez-Semadeni et al. 2005; Nakamura & Li 2007). This may affect the kinetic energies observed in the clumps, and we plan to repeat the present analysis in a future contribution including

both feedback and magnetic fields. Nevertheless, the similarity of the distribution of clumps in our simulations in the KH diagram to the observed one suggests that these agents may only play a secondary role during the assembly and early stages of collapse of clumps and cores.

4.2. Applicability to low- and high-mass regions

Strictly speaking, our results only apply to low-mass clumps and cores, since our sample does not include high-mass, high-column density (high-Σ) objects (see, e.g., the bottom panels of Fig. 4) similar to cluster- forming clumps, such as those studied by Fall et al. (2010). Nevertheless, because massive-star forming cores do appear to follow the same scaling in the KH (e.g., Ballesteros-Paredes et al. 2011, Ballesteros-Paredes et al. 2016, in preparation) diagram as MCs and the low-mass cores we have discussed in Sec. 3.2, we speculate that our results may apply to high-mass, high-Σ clumps. The clumps examined by Fall et al. (2010), which were selected for their star formation activity (not for their volume or surface density) have masses in the range $10^2 \lesssim M \lesssim 10^6 M_\odot$ and surface densities $\Sigma \sim 10^3 M_\odot \mathrm{pc}^{-2}$. They are currently experiencing strong stellar feedback that may counteract with their own self-gravity. The fact that these clumps have roughly constant column density may indicate that these values of Σ are physically selected by the requirement of exhibiting strong star formation and feedback. Column densities much higher than $\sim 10^3 M_\odot \mathrm{pc}^{-2}$ may not be observed because at that point gas removal from the clumps becomes important (Fall et al. 2010). On the other hand, at column densities lower than those values, the star formation activity may not be so strong (Zamora-Avilés et al. 2012; Zamora-Avilés & Vázquez-Semadeni 2014), and the association between the gas and the stars may not be one-to-one because of the longer collapse timescales involved at lower densities (Burkert & Hartmann 2013), and thus lower-column density objects will not be selected by a strong star formation activity criterion.

4.3. Comparison with previous work

Our results can be compared with those obtained in two recent papers that have performed numerical simulations of supernova (SN)-driven turbulence in the ISM, one in a $(250\ \mathrm{pc})^3$ cubic box (Padoan et al. 2016, hereafter P+16), the other in a parallelepiped-shaped box of $1\times1\times40\ \mathrm{kpc}^3$, with a vertically stratified medium (Ibáñez-Mejía et al. 2016, hereafter IM+16). In both cases, turbulence is driven for some time before turning on self-gravity. These two papers have arrived at opposite conclusions concerning the distribution of the simulated clouds in the KH diagram: IM+16 find that the MC-like objects in their simulation develop near-equipartition after turning on self-gravity, while P+16 find that their clouds never approach equipartition, and instead have a roughly constant value of the ratio $\mathcal{H} \equiv \sigma_\mathrm{v}/R^{1/2}$, independent of the column density Σ, suggesting that Larson's linewidth-size relation is valid after all, and equipartition is not. They also show that a sample of outer-Galaxy clouds (Heyer et al. 2001) appears to be consistent with this result.

The results from our initially random-driven, and subsequently decaying simulations support those of IM+16 but not those of P+16, since our clouds and clumps in general approach the equipartition state. Moreover, we find that equipartition is more tightly fulfilled at higher column densities, while low-column density objects exhibit larger kinetic energy excesses over equipartition, in agreement with observational data from various observational surveys (e.g., Barnes et al. 2011; Leroy et al. 2015). Nevertheless, the most massive of the low-column density objects are the ones closest to equipartition, suggesting that the motions are dominated by gravity.

The origin of the contrasting results between IM+16 and P+16, both from their respective simulations and from the observations each group considered, deserves further examination. Concerning the simulations, ample discussion has been given by IM+16, and here we just point out that the simulations of P+16 may suffer from significant overdriving of the turbulence. This is because they apply a standard value of the SN surface density rate ($\sim 100\ \mathrm{Myr}^{-1}\ \mathrm{kpc}^{-2}$) into their $(250\ \mathrm{pc})^3$ numerical box. Although indeed most SN explosions are expected to occur within this vertical span around the Galactic midplane, the short height of the simulation box, which uses periodic boundaries, does not allow the energy injected by the SNe to escape to high altitudes, and to drive a galactic fountain,

as it is known to do. Instead, this energy must remain within the small volume of the simulation, likely overdriving the turbulence in comparison with the actual observed levels in the ISM. For example, Figure 6 in P+16 shows that the mean whole-box velocity dispersion increases steadily from ~ 20 to ~ 100 km s^{-1} during the last 10 Myr of evolution shown. However, Scannapieco et al. (2012, see also Gatto et al. 2015) have recently found that in simulations where the total velocity dispersion exceeds ~ 35 km s^{-1}, the medium goes into a thermal runaway regime where the gas is shocked into an unstable regime in which the cooling time increases strongly with temperature, causing a substantial fraction of the ISM to be unable to cool on a turbulence dissipation timescale. As a consequence, the medium goes into runaway heating, causing ejection of gas from any stratified medium. Since the simulation by P+16 lacks such stratification, the simulation is probably just heating up, explaining the continuous rise of the velocity dispersion, and justifying our interpretation that this simulation is overdriven and therefore not very realistic for the purpose of examining the energy budget of the clumps.

On the other hand, concerning the outer-Galaxy cloud data used by P+16, it is important to remark that these clouds have in general quite low column densities, in the range 10–100 $M_\odot$ pc^{-2}. Thus, they are indeed in the column density range where our simulations indicate that turbulence is still dominant (see Fig. 5), even if, as clouds grow, they may later transition to being dominated by self-gravity. In fact, the outer-Galaxy sample has been plotted by Leroy et al. (see Fig. 13 of 2015) together with data from several other surveys, and it can be seen that the outer-Galaxy clouds have the lowest-column densities and the largest scatter in the $\mathcal{H}$ parameter of the whole dataset, as with our results for the low-column density clouds in our simulations. Nevertheless, when one considers the whole dataset, including in particular objects of substantially larger column densities, the tendency towards equipartition is recovered, as shown in Figure 13 of Leroy et al. (2015) and our own Fig. 5. We therefore conclude that both the simulations and the data considered by P+16 are restricted to regimes where indeed turbulence is dominant (either by too strong turbulence driving or a low column density of the clouds), but that these do not represent the general trend in the Galactic ISM when a wide range of column densities is considered.

5. Summary and conclusions

In this paper we have investigated the intrinsic (rather than derived from synthetic observations) physical conditions of clumps and cores in two SPH simulations of the formation and evolution of molecular clouds formed by converging motions in the warm neutral medium (WNM). The two simulations attempt to span a range of likely motions in this medium.

In both simulations, once the dense clouds form, they soon begin to contract gravitationally, and some time later (a few Myr) they begin to form stars, as in the general scenario described by Vázquez-Semadeni et al. (2007) and Heitsch & Hartmann (2008). Neither of the simulations includes turbulence-driving stellar feedback nor magnetic fields, and so all of the kinetic energy is either driven by gravity or is a residual of the turbulent/compressive motions that initiated the formation of the clouds. Within this context of globally contracting molecular clouds (MCs), we have investigated whether the clumps within them follow the Larson scaling relations, or their generalization, as proposed by H09 and B11. We have also investigated the physical conditions in clumps that appear to have an excess of kinetic energy, in an attempt to understand the physical processes that cause this apparent over-virialization.

We created an ensemble of clumps in each simulation by defining clumps as connected sets of SPH particles above a certain density-threshold $n_{\rm th}$, so that a single clump at a lower threshold may contain several clumps at a higher value of $n_{\rm th}$. The objects defined at the highest thresholds ($n_{\rm th} \geq 10^5$ cm^{-3}) are refereed to as "cores".

Our results and conclusions may be summarized as follows:

- The full ensemble of clouds, clumps and cores does not follow either of the Larson scaling relations, but mostly follows their generalization, as proposed by H09 and B11. Nevertheless, low column density clumps in particular exhibit a large scatter, with a significant fraction of the clumps having val-

ues of the $\mathcal{H} \equiv \sigma_{\rm v}/R^{1/2}$ parameter of up to an order of magnitude larger than the virial value, similar to the situation in various observational studies.

- We noted that, as emphasized by B11, the kinetic energy implied by free-falling motions is only a factor of $\sqrt{2}$ larger than that for virial equilibrium. We therefore generically refer to this condition as "energy equipartition".

- In our simulations, the equipartition condition is due to gravitational contraction, by construction.

- The clumps defined at a single threshold $n_{\rm th}$ do not exhibit density-size or velocity dispersion-size relations. Instead, the exhibit nearly constant volume density, in agreement with previous studies (Ballesteros-Paredes & Mac Low 2002). However, ensembles of clumps that exhibit near-equipartition and that are selected by column density ranges, do exhibit Larson-like relations, suggesting that these relations are special cases of the more general equipartition condition.

- We find examples of clouds, clumps and cores that exhibit excess kinetic energies over the equipartition level at both low- and high-column densities. Low-column density clumps that exhibit this excess are the least massive, while the more massive ones are closer to equipartition. Moreover, for more than 50% of the low-density clumps with an $\mathcal{H}$ excess in both simulations, the velocity field in the clouds appears to be convergent (i.e. have negative net divergence). This suggests an evolutionary process in which a turbulent compression initially dominates the kinetic energy and exceeds the gravitational energy of the forming cloud. However, as the cloud becomes denser and more massive, the gravitationally-driven velocity becomes dominant. Also, this suggests that the observation of an excess kinetic energy does not necessarily imply that a clump will disperse or needs an external thermal confining pressure to avoid dispersal. The excess kinetic energy may simply reflect the initial compressive motions within the clump. In this case, instead of *confinement* of the cores by thermal pressure, we have *assembly* by ram pressure.

- Some of the high-column density cores that exhibit kinetic energy excesses contain stellar particles that increase the total gravitational potential in the volume of the clump. When this stellar mass is added to the gas mass in the energy budget of the core, the gas+stars system returns to near equipartition.

- Some high-column density clumps with kinetic energy excesses, however, do not contain stellar particles, so that the the above correction cannot be applied. Investigation of the velocity field in these cases does show a rotating and/or expanding motion, so that these objects are in the process of being disrupted, and will not form stars. Because this process is occurring at high densities, the driver of these disrupting motions is likely to be the turbulence generated by the large-scale collapse.

- We also investigated the possibility that excess kinetic energies in high-column density cores might be due to the cores being located in filamentary clumps, with net accretion from the filament onto the core, so that the velocity dispersion in the cores might represent the gravitational potential of the mass in the filament. However, this mechanism does not seem to be operational. We find that the filaments and their embedded cores begin their evolution roughly simultaneously, accreting material from the cloud mostly perpendicularly to the filament. Accretion from the filament onto the core begins later, when the core has become more massive and has already started to form stars. Thus, cores that are actively accreting from their parent filaments are already in advanced star-forming stages, and do not correspond to pre- or early protostellar objects.

The numerical simulations were produced in the cluster acquired through CONACYT grant 102488

to E.V.-S. JBP acknowledges financial support from UNAM-PAPIIT grant number IN110816.

REFERENCES

Abel, T. 2011, MNRAS, 413, 271

André, P., Men'shchikov, A., Bontemps, S., et al. 2010, A&A, 518, L102

Audit, E., & Hennebelle, P. 2005, A&A, 433, 1

Audit, E., & Hennebelle, P. 2010, A&A, 511, A76

Ballesteros-Paredes, J., D'Alessio, P., & Hartmann, L. 2012, MNRAS, 427, 2562

Ballesteros-Paredes, J., Hartmann, L. W., Vázquez-Semadeni, E., Heitsch, F., & Zamora-Avilés, M. A. 2011, MNRAS, 411, 65 (B11)

Ballesteros-Paredes, J., & Mac Low, M.-M. 2002, ApJ, 570, 734 (BM02)

Barnes, P. J., Yonekura, Y., Fukui, Y., et al. 2011, ApJS, 196, 12

Bate, M. R., & Burkert, A. 1997, MNRAS, 288, 1060

Beaumont, C. N., Goodman, A. A., Alves, J. F., et al. 2012, MNRAS, 423, 2579

Bertoldi, F., & McKee, C. F. 1992, ApJ, 395, 140

Blitz, L. 1993, Protostars and Planets III, 125

Blitz, L., & Williams, J. P. 1999, NATO Advanced Science Institutes (ASI) Series C, 540, 3

Burkert, A., & Hartmann, L. 2013, ApJ, 773, 48

Caselli, P., & Myers, P. C. 1995, ApJ, 446, 665

Colín, P., Vázquez-Semadeni, E., & Gómez, G. C. 2013, MNRAS, 435, 1701

Crutcher, R. M. 2012, ARA&A, 50, 29

Dale, J. E., Ercolano, B., & Bonnell, I. A. 2012, MNRAS, 424, 377

de Avillez, M. A., & Breitschwerdt, D. 2004, A&A, 425, 899

C. L. Dobbs, A. Burkert, and J. E. Pringle 2011, MNRAS, 413

Elmegreen, B. G., & Scalo, J. 2004, ARA&A, 42, 211

Fall, S. M., Krumholz, M. R., & Matzner, C. D. 2010, ApJ, 710, L142

Field, G. B., Blackman, E. G., & Keto, E. R. 2011, MNRAS, 416, 710

Gatto, A., Walch, S., Low, M.-M. M., et al. 2015, MNRAS, 449, 1057

Gazol, A., Vázquez-Semadeni, E., & Kim, J. 2005, ApJ, 630, 911

Gazol, A., & Kim, J. 2013, ApJ, 765, 49

Gibson, D., Plume, R., Bergin, E., Ragan, S., & Evans, N. 2009, ApJ, 705, 123

Goldreich, P., & Kwan, J. 1974, ApJ, 189, 441

Gómez, G. C., & Vázquez-Semadeni, E. 2014, ApJ, 791, 124

Gong, M., & Ostriker, E. C. 2015, ApJ, 806, 31

González-Samaniego, A., Vázquez-Semadeni, E., González, R. F., & Kim, J. 2014, MNRAS, 440, 2357

Hartmann, L., Ballesteros-Paredes, J., & Bergin, E. A. 2001, ApJ, 562, 852

Heiles, C., & Troland, T. H. 2003, ApJ, 586, 1067

Heiner, J. S., Vázquez-Semadeni, E., & Ballesteros-Paredes, J. 2015, MNRAS, 452, 1353

Heitsch, F., Burkert, A., Hartmann, L. W., Slyz, A. D., & Devriendt, J. E. G. 2005, ApJ, 633, L113

Heitsch, F., & Hartmann, L. 2008, ApJ, 689, 290

Heitsch, F., Hartmann, L. W., Slyz, A. D., Devriendt, J. E. G., & Burkert, A. 2008, ApJ, 674, 316

Heitsch, F., Slyz, A. D., Devriendt, J. E. G., Hartmann, L. W., & Burkert, A. 2006, ApJ, 648, 1052

Hennebelle, P., Banerjee, R., Vázquez-Semadeni, E., Klessen, R. S., & Audit, E. 2008, A&A, 486, L43

Hennebelle, P., & Pérault, M. 1999, A&A, 351, 309

Heyer, M. H., Carpenter, J. M., & Snell, R. L. 2001, ApJ, 551, 852

Heyer, M. H., & Brunt, C. M. 2004, ApJ, 615, L45

Heyer, M., Krawczyk, C., Duval, J., & Jackson, J. M. 2009, ApJ, 699, 1092, (H09)

Heyer, M., & Dame, T. M. 2015, ARA&A, 53, 583

Ibáñez-Mejía, J. C., Mac Low, M.-M., Klessen, R. S., & Baczynski, C. 2016, ApJ, 824, 41

Jackson, J. M., Rathborne, J. M., Shah, R. Y., et al. 2006, ApJS, 163, 145

Jappsen, A.-K., Klessen, R. S., Larson, R. B., Li, Y., & Mac Low, M.-M. 2005, A&A, 435, 611

Kegel, W. H. 1989, A&A, 225, 517

Keto, E. R., & Myers, P. C. 1986, ApJ, 304, 466

Kirk, H., Myers, P. C., Bourke, T. L., et al. 2013, ApJ, 766, 115

Klessen, R. S., & Hennebelle, P. 2010, A&A, 520, A17

Koyama, H., & Inutsuka, S.-i. 2002, ApJ, 564, L97

Lada, C. J., & Lada, E. A. 2003, ARA&A, 41, 57

Larson, R. B. 1981, MNRAS, 194, 809

Leroy, A. K., Bolatto, A. D., Ostriker, E. C., et al. 2015, ApJ, 801, 25

Liszt, H. S., Wilson, R. W., Penzias, A. A., et al. 1974, ApJ, 190, 557

Lombardi, M., Alves, J., & Lada, C. J. 2010, A&A, 519, L7

Lombardi, M., Alves, J., & Lada, C. J. 2015, A&A, 576, L1

Louvet, F., Motte, F., Hennebelle, P., et al. 2014, A&A, 570, A15

Matzner, C. D., & McKee, C. F. 2000, ApJ, 545, 364

McKee, C. F., & Ostriker, E. C. 2007, ARA&A, 45, 565

Nakamura, F., & Li, Z.-Y. 2007, ApJ, 662, 395

Ostriker, E. C., Gammie, C. F., & Stone, J. M. 1999, ApJ, 513, 259

Padoan, P., Pan, L., Haugbølle, T., & Nordlund, Å. 2016, ApJ, 822, 11

Palau, A., Fuente, A., Girart, J. M., et al. 2013, ApJ, 762, 120

Pan, L., Padoan, P., Haugbolle, T., & Nordlund, A. 2015, arXiv:1510.04742

Peretto, N., Fuller, G. A., Duarte-Cabral, A., et al. 2013, A&A, 555, A112

Plume, R., Jaffe, D. T., Evans, N. J., II, Martín-Pintado, J., & Gómez-González, J. 1997, ApJ, 476, 730

Pon, A., Toalá, J. A., Johnstone, D., et al. 2012, ApJ, 756, 145

Scalo, J. 1990, Physical Processes in Fragmentation and Star Formation, 162, 151

Scannapieco, E., Gray, W. J., & Pan, L. 2012, ApJ, 746, 57

Schneider, N., Csengeri, T., Bontemps, S., et al. 2010, A&A, 520, A49

Shirley, Y. L., Evans, N. J., II, Young, K. E., Knez, C., & Jaffe, D. T. 2003, ApJS, 149, 375

Solomon, P. M., Rivolo, A. R., Barrett, J., & Yahil, A. 1987, ApJ, 319, 730

Springel, V., Yoshida, N., & White, S. D. M. 2001, New A, 6, 79

Toalá, J. A., Vázquez-Semadeni, E., & Gómez, G. C. 2012, ApJ, 744, 190

Traficante, A., Fuller, G. A., Smith, R., et al. 2015, arXiv:1511.03670

Vázquez-Semadeni, E. 2015, Astrophysics and Space Science Library, 407, 401

Vázquez-Semadeni, E., Ballesteros-Paredes, J., & Rodríguez, L. F. 1997, ApJ, 474, 292

Vázquez-Semadeni, E., Colín, P., Gómez, G. C., Ballesteros-Paredes, J., & Watson, A. W. 2010, ApJ, 715, 1302

Vázquez-Semadeni, E., Gazol, A., & Scalo, J. 2000, ApJ, 540, 271

Vázquez-Semadeni E., Gómez G. C., Jappsen A.-K., Ballesteros-Paredes J., González R. F., Klessen R. S., 2007, ApJ, 657, 870

Vázquez-Semadeni E., Gómez G. C., Jappsen A.-K., Ballesteros-Paredes J., Klessen R. S., 2009, ApJ, 707, 1023

Vázquez-Semadeni, E., González, R. F., Ballesteros-Paredes, J., Gazol, A., & Kim, J. 2008, MNRAS, 390, 769

Vázquez-Semadeni, E., Kim, J., & Ballesteros-Paredes, J. 2005, ApJ, 630, L49

Vázquez-Semadeni, E., Kim, J., Shadmehri, M., & Ballesteros-Paredes, J. 2005, ApJ, 618, 344

Vázquez-Semadeni, E., Ostriker, E. C., Passot, T., Gammie, C. F., & Stone, J. M. 2000, Protostars and Planets IV, 3

Vázquez-Semadeni, E., Ryu, D., Passot, T., González, R. F., & Gazol, A. 2006, ApJ, 643, 245

Williams, J. P., de Geus, E. J., & Blitz, L. 1994, ApJ, 428, 693

Wu, J., Evans, N. J., II, Shirley, Y. L., & Knez, C. 2010, ApJS, 188, 313

Zamora-Avilés, M., & Vázquez-Semadeni, E. 2014, ApJ, 793, 84

Zamora-Avilés, M., Vázquez-Semadeni, E., & Colín, P. 2012, ApJ, 751, 77

Zuckerman, B., & Evans, N. J., II 1974, ApJ, 192, L149

Zuckerman, B., & Palmer, P. 1974, ARA&A, 12, 279

This 2-column preprint was prepared with the AAS LaTeX macros v5.2.